Version of Record at: https://doi.org/10.1364/OL.486595

Optics Letters

Micro-dispenser-based optical packaging scheme for grating couplers

S. M. Zia Uddin,[1,†] Ellen Gupta,[1,†] Masudur Rahim,[1] Zi Wang,[1] Yang Du,[2] Kaleem Ullah,[1] Craig B. Arnold,[2,3] Mark Mirotznik,[1] and Tingyi Gu[1,*]

[1]Department of Electrical Engineering, University of Delaware, Newark, Delaware 19711, USA
[2]Princeton Institute for the Science and Technology of Materials, Princeton University, Princeton, New Jersey 08540, USA
[3]Department of Mechanical and Aerospace Engineering, Princeton University, Princeton University, Princeton, New Jersey 08540, USA
[†]These authors contributed equally to this work.
[*]tingyigu@udel.edu

Received 30 January 2023; revised 27 February 2023; accepted 12 March 2023; posted 21 March 2023; published 13 April 2023

Due to their sub-millimeter spatial resolution, ink-based additive manufacturing tools are typically considered less attractive than nanophotonics. Among these tools, precision micro-dispensers with sub-nanoliter volumetric control offer the finest spatial resolution: down to 50 μm. Within a sub-second, a flawless, surface-tension-driven spherical shape of the dielectric dot is formed as a self-assembled μlens. When combined with dispersive nanophotonic structures defined on a silicon-on-insulator substrate, we show that the dispensed dielectric μlenses [numerical aperture (NA) = 0.36] engineer the angular field distribution of vertically coupled nanostructures. The μlenses improve the angular tolerance for the input and reduces the angular spread of the output beam in the far field. The micro-dispenser is fast, scalable, and back-end-of-line compatible, allowing geometric-offset-caused efficiency reductions and center wavelength drift to be easily fixed. The design concept is experimentally verified by comparing several exemplary grating couplers with and without a μlens on top. A difference of less than 1 dB between incident angles of 7° and 14° is observed in the index-matched μlens, while the reference grating coupler shows around 5 dB contrast.

© 2023 Optica Publishing Group under the terms of the Optica Open Access Publishing Agreement

https://doi.org/10.1364/OL.486595

Integrated photonics implement complex photonic systems in small chiplets, including optical trapping [1–3], biosensing [4,5], quantum optics [6,7], and optical phase arrays for free-space beam steering [8]. As the on/off-chip interface is critical, many efforts have been dedicated to improving the performance of couplers such as tapers [9–14], lensed fiber [15–17], and directly coupled on-chip facets [18]. Near-unity coupling efficiency has been demonstrated for grating couplers with fabrication steps far beyond traditional foundry compliance [19–24]. Simultaneously achieving the desired beam shape, low insertion loss, and the target operation wavelength may be beyond the capacity of the in-plane design parameter space, which can be compensated for by using out-of-plane design space [25,26]. An additional layer of metasurface on top of the grating coupler shapes the output beam to achieve the desired direction and spread [27]. Three-dimensional (3D) direct laser writing (DLW) with nanometer spatial resolution has pioneered the optical packaging of high-contrast nanophotonics, including freeform 3D optical couplers for integrated photonics [28–33]. Polymer-based couplers guide the mode conversion from the sub-micrometer area in a single-mode waveguide to fiber (~10 μm diameter), delivering broadband (>100 nm) and low insertion loss (<1 dB) coupling. Potential concerns with 3D DLW include a slow printing speed (a few months for 10^5 couplers per wafer) and additional scattering. Complementary to DLW, ink-jet printing is an alternative additive manufacturing (AM) tool with high throughput [34–36]. With the advancement of technology, precision micro-dispensing with sub-nanoliter volumetric control offers the finest resolution among these solution-based printing tools, and features high throughput (5 dots per second). It has been widely adopted in micro-electronic packaging, printed electronics, and biomanufacturing, but its photonic applications are underexplored. Here we demonstrate the advanced photonic functions enabled by the combination of AM micro-dispensing and nanofabrication.

The design concept was experimentally implemented with ebeam lithography-led nanophotonic fabrication and micro-dispensing [Fig. 1(a)]. The grating coupler was fabricated on a silicon-on-insulator (SOI) (100) substrate from Soitec, with a 250 nm device layer on a 3 μm silicon dioxide layer. The designed patterns (e.g., waveguides, grating couplers) were defined in the positive resist, followed by resist development and single-step dry etch procedures. A thin (less than 20 nm) silicon dioxide protection layer was deposited on the device layer by plasma-enhanced chemical vapor deposition [36]. To print the μlenses, an AM approach was taken via the nScrypt 3Dn-300 [Figs. 1(b) and 1(c)]. Refractive-index-matched UV-epoxy ($n = 1.55$) was then deposited on the grating coupler through a micro-dispensing process. The nScrypt 3Dn-300 provided subnanoliter volumetric control of the UV-curable one-part adhesive. A nozzle diameter of 25 μm was employed to achieve diameters ranging from 50 to 150 μm by controlling the open duration of the valve system (0.01–0.05 s). A print command was then generated to open the valve of the dispensing tool for

Version of Record at: https://doi.org/10.1364/OL.486595

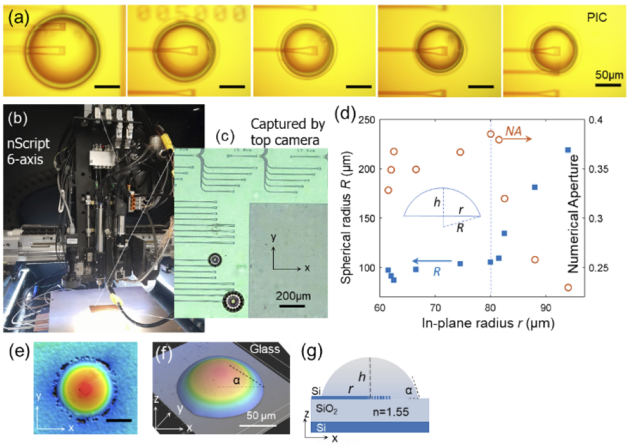

Fig. 1. Micro-dispenser-printed micro-lenses on grating couplers. (a) Exemplary micro-droplets of lenses prepared by AM, with the droplet in-plane radius varying between 50 and 100 μm. Their centers are aligned with grating couplers defined on an SOI substrate. Optical images of (b) the printer and (c) the photonic integrated circuits under the printer, captured by the top camera installed on the printer. (d) Measured spherical radius R versus measured in-plane radius r for the 10 micro-lenses produced by the dispenser. Right y axis: corresponding numerical aperture. (e) Top view and (f) perspective view of the measured 3D profile of a μlens with refractive index matching gel ($n = 1.55$) by profilometry. Scale bar: 50 μm. (g) Schematic cross section of a device. The numerical aperture of the μlens is set by the contact angle (α) at the interface.

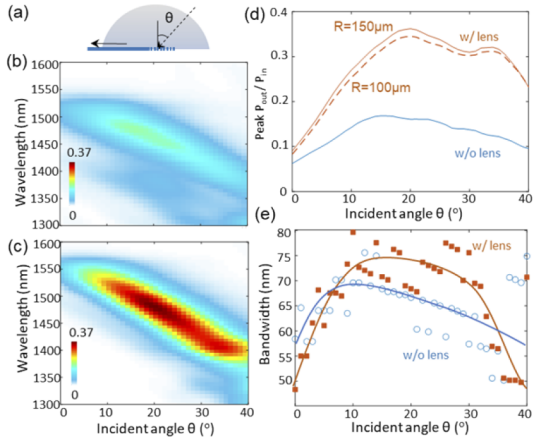

Fig. 2. μlens-modified fiber–chip coupling spectra. (a) Cross-sectional schematic indicating the incident angle θ. Transmission spectrum versus incident angle for (b) the adiabatic grating coupler defined on SOI and (c) the same device with a μlens. (d) Peak transmission versus incident angle at the optimal transmission wavelengths in (b) and (c) obtained without (blue) and with (orange) a μlens. (e) Extracted full width at half maximum bandwidth of the transmission spectrum versus the incident angle for both conditions.

0.5 seconds and then close it to lay down the adhesive without drooling. No heat was applied to the print nozzle or print bed. After dispensing the μlens array, temporary curing was applied by a UV flashlight (wavelength of 365 nm at 15 W) for 1 minute for rapid solidification and to avoid deformation during the movement. Then the sample was removed from the print bed and placed in a UV light chamber for 25 minutes to fully cure the lens (wavelength of 365 nm at 93 mW/cm^2).

The cross-sectional profiles of the μlenses were measured by comparing the results obtained from an imaging surface profiler and a surface profilometer. The former provided a 3D contour of the surface and the latter provided a one-dimensional (1D) contour with higher precision. A laser confocal microscope system, the Keyence VK-X3000 3D surface profiler characterized the top profile of each μlens [Figs. 1(e) and 1(f)], examining the imperfections and roughly estimating the in-plane radius (r) and height (h). Then we selected a few exemplary μlenses to accurately measure the r and h under a Dektak surface profilometer. The curvature R [see the inset of Fig. 1(d)] can be derived as: $R = \frac{h}{2} + \frac{r^2}{2h}$. Given the cured polymer refractive index (n) and R, we estimated the focal length f and the numerical aperture (NA) of each μlens using $f = \frac{R}{n-1}$ and $\mathrm{NA} = \frac{1}{\sqrt{1+(f/r)^2}}$, where $\frac{f}{r} = \frac{1}{2(n-1)}\left(\frac{h}{r} + \frac{r}{h}\right)$. The contact angle between the UV polymer and SOI substrate α is set by the interface interaction and viscosity of the polymer: $r = R\sin\alpha$ [35]. After replacing R with the expression containing h and r, we derive $\frac{2}{\sin\alpha} = \frac{h}{r} + \frac{r}{h}$. After substituting this factor into the expression for NA, we obtain

$$\mathrm{NA} = \frac{1}{\sqrt{1 + \left(\frac{1}{\sin\alpha(n-1)}\right)^2}}. \quad (1)$$

Equation (1) reveals that NA should be independent of the droplet size r. The lack of dependence of NA on r was experimentally verified for multiple droplets [Fig. 1(d)]. For the droplets with an in-plane radius r of less than 80 μm, the NA stays around 0.36 [orange circles in Fig. 1(d)], and the curvature or spherical radius R remains around 100 μm [blue squares in Fig. 1(d)]. The size-independent NA aligns with the numerical prediction in Eq. (1), where the contact angle α is derived to be 0.78 rad on the glass surface [Fig. 1(d)]. Larger droplets result in a reduced NA. As r can be simplified and quantified under an optical microscope, it can be used to quickly estimate the NA values of newly prepared droplets.

Numerical evaluation of the index-matched μlens atop the grating coupler was performed by the 3D finite-difference-time-domain method (FDTD). The grating couplers' settings were fully etched and anodized as the ones in fabrication [Fig. 1(a)]. By varying the fiber incident angle (θ) [Fig. 2(a)], we examined the transmission spectra of the grating coupler before [Fig. 2(b)] and after adding the μlens [$R = 100$ μm, Fig. 2(c)]. In grating-coupler-only substrates, the FDTD-simulated peak efficiency is 15% at an incident angle of 15° [blue curve in Fig. 2(d)]. Note that the peak wavelength varies with the incident angle [Figs. 2(b) to 2(c)]. With a similar parameter sweep from 0° to 40°, the same grating coupler design with a μlens on top shows a maximum transmission of around 35% at 20°. It is noted that the 20% enhancement of the peak transmission is mostly attributed to the h adjustment. An increased full width at half maximum bandwidth (10–20 nm) is observed at incident angles between 10° and 30°, which is attributed to the curvature of the μlens [Fig. 2(e)].

As an example, we compared their transmission spectra at incident angles of 7° and 14° [Figs. 3(a) and 3(b)]. For the given design of a fully etched grating coupler [37] defined in 250 nm SOI substrate, peak transmission of near to 20% is obtained at both incident angles [blue curves in Fig. 2(a)]. The μlens on top increases the transmission peak to 36% and 42% for incident

Version of Record at: https://doi.org/10.1364/OL.486595

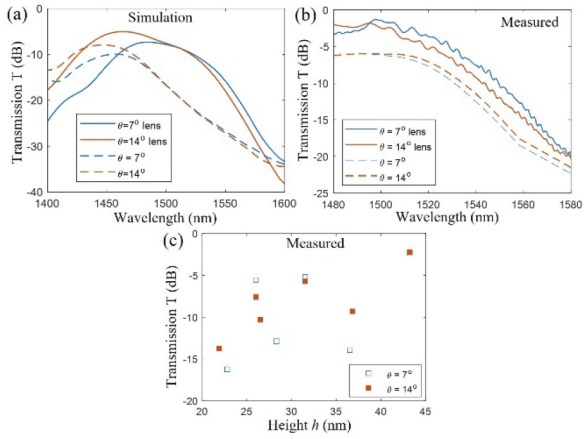

Fig. 3. Measured optical characteristics. (a) Numerically predicted and (b) measured transmission spectra of the μlens atop a grating coupler with (orange) and the same design without a μlens (blue) at the incident angles of 7° (dashed curves) and 14° (solid curves). (c) Peak transmission of a μlens atop a grating coupler versus the height of the μlens for an incident angle of 7° (blue) and 14° (orange).

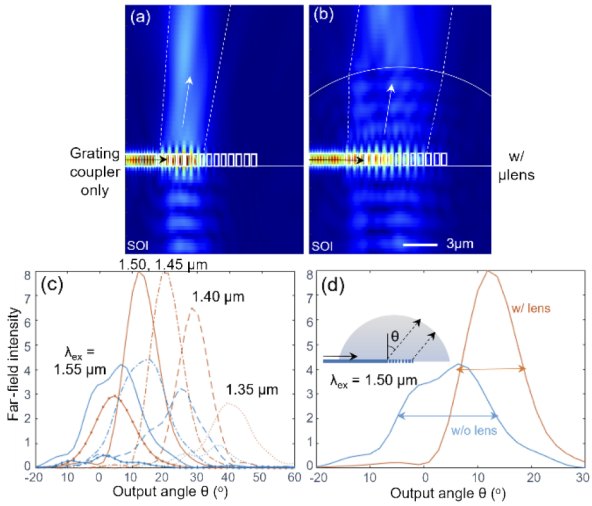

Fig. 4. μlens-modified far-field projection for dispersion-based beam steering. Cross-sectional views of the grating coupler with in-waveguide excitations (a) before and (b) after adding the μlens ($R = 100$ μm, $h = 2.75$ μm). (c) Incident-wavelength-dependent far-field projection for a bare grating coupler (blue) and a grating coupler with a μlens (yellow). (d) Selective far-field projection at an input laser wavelength of 1.50 μm (at a distance of 1 m).

angles of 7° and 14°, respectively (orange curves). Experimentally, we prepared 11 μlenses atop grating couplers and compared their angle-dependent transmission spectra to those of another 11 samples with identical grating coupler designs [Fig. 1(d)]. A precision angle controller (Thorlabs Nanomax 300) was used to fine-tune the incident angle of the single-mode fiber between 5° and 15°. A tunable laser fed continuous waves to the chip through a polarization controller. The output light from the grating coupler was collected by another single-mode fiber (fixed angle) and sent to a power meter. We plot the peak transmission of the μlens atop the grating coupler versus the height h in Fig. 3(c). Transmission increases with h for both incident angles. Note that the fluctuations in transmission intensity are due to fabrication variation and misalignment of the μlens. Here the μlenses were manually aligned, and the center misalignment was less than 2 μm. Numerical studies show that the efficiency variation is less than 2.5% for misalignment of ±3 μm in the y direction and ±1 μm in the x direction. A steep drop (>5%) in coupling efficiency is observed for misalignment of ±4 μm in the y direction and ±2 μm in the x direction.

Then we explored the use of the grating couplers as emitters in the near and far fields (Fig. 4). With the laser wavelength placed at the peak of the transmission, cross-sectional views of in-plane to out-of-plane light conversion before [Fig. 4(a)] and after [Fig. 4(b)] adding the μlens were compared. Without the top cladding layer, the optical field is confined in the first half of the grating coupler (10 μm length in total). The angular spread in the far field is plotted in Fig. 4(c) (blue curves). Depending on the input laser wavelength, the peak angle can vary from 0° to 40°. As it is the inverse process to fiber–chip coupling [Fig. 2(d)], the far-field peak transmission increases with the μlens cladding as well [orange curves in Fig. 4(c)]. The curve surface helps to reduce the angular spread, as illustrated in Fig. 4(b), which results in a reduced spot size in the far field. At an incident wavelength of 1.5 μm, a nearly 50% reduction in the angular spread is expected [Fig. 4(d)].

In this work, we explored the feasibility of using an ink-based AM method for the optical packaging of grating couplers. The micro-dispenser approach allows high throughput, has a relatively low cost, and is compatible with back-end-of-line processing in silicon photonic foundry manufacturing. In addition to reducing the insertion loss, the contact-angle-defined NA of the μlens is around 0.36, which expands the angle tolerance of the input fiber and suppresses the angular spread of the output beam from the grating coupler in the far field. We experimentally measured the NA of a micro-droplet dispensed on SOI substrate and characterized the transmission spectra of exemplary grating couplers before and after adding the μlens. In particular, the μlenses atop grating couplers were more tolerant of the fiber incident angle deviation. This fully automated and high-throughput micro-dispenser is capable of printing on large arrays of grating couplers (typically 10^5 couplers) on an 8-inch wafer within 5.5 hours, compared to 2 months of continuous writing for DLW.

Funding. Semiconductor Research Corporation; University of Delaware Research Foundation; Defense Advanced Research Projects Agency (N660012114034).

Acknowledgments. The authors are grateful for the discussions with Dr. Justin Bickford and Dr. Pak Cho from the Army Research Laboratory at Adelphi. This work was supported in part by COGNISENSE, one of seven centers in JUMP 2.0, a Semiconductor Research Corporation (SRC) program sponsored by the Defense Advanced Research Projects Agency.

Disclosures. The authors declare no conflicts of interest.

Data availability. The data that support the findings of this study are available on request from the corresponding author.

REFERENCES

1. D. Conteduca, G. Brunetti, G. Pitruzzello, F. Tragni, K. Dholakia, T. F. Krauss, and C. Ciminelli, ACS Photonics **8**, 2060 (2021).
2. R. J. Niffenegger, J. Stuart, C. Sorace-Agaskar, D. Kharas, S. Bramhavar, C. D. Bruzewicz, W. Loh, R. T. Maxson, R. McConnell, D. Reens, and G. N. West, Nature **586**, 538 (2020).

Version of Record at: https://doi.org/10.1364/OL.486595

3. K. K. Mehta, C. Zhang, M. Malinowski, T.-L. Nguyen, M. Stadler, and J. P. Home, Nature **586**, 533 (2020).
4. M. C. Estevez, M. Alvarez, and L. M. Lechuga, Laser Photonics Rev. **6**, 463 (2012).
5. G. B. Loozen, A. Karuna, M. M. R. Fanood, E. Schreuder, and J. Caro, Beilstein J. Nanotechnol. **11**, 829 (2020).
6. X. Qiang, X. Zhou, J. Wang, C. M. Wilkes, T. Loke, S. O'Gara, L. Kling, G. D. Marshall, R. Santagati, T. C. Ralph, J. B. Wang, J. L. O'Brien, M. G. Thompson, and J. C. F. Matthews, Nat. Photonics **12**, 534 (2018).
7. J. Wang, S. Paesani, Y. Ding, R. Santagati, P. Skrzypczyk, A. Salavrakos, J. Tura, R. Augusiak, L. Mančinska, D. Bacco, D. Bonneau, J. W. Silverstone, Q. Gong, A. Acín, K. Rottwitt, L. K. Oxenløwe, J. L. O'Brien, A. Laing, and M. G. Thompson, Science **360**, 285 (2018).
8. Y. Liu and H. Hu, Optica **9**, 903 (2022).
9. R. M. Reano and P. Sun, Proc. SPIE **7606**, 76060J (2010).
10. K. Shiraishi, H. Yoda, and C. S. Tsai, Opt. Express **20**, 24370 (2012).
11. A. Khilo, M. A. Popović, M. Araghchini, and F. X. Kärtner, Opt. Express **18**, 15790 (2010).
12. H. Park, S. Kim, J. Park, J. Joo, and G. Kim, Opt. Express **21**, 29313 (2013).
13. K.-N. Ku and M.-C. M. Lee, J. Lightwave Technol. **31**, 1616 (2013).
14. R. H. Khandokar, M. Bakaul, M. Asaduzzaman, A. Nirmalathas, and S. Skafidas, IEEE J. Quantum Electron. **52**, 1 (2016).
15. G. Ren, S. Chen, Y. Cheng, and Y. Zhai, Opt. Commun. **284**, 4782 (2011).
16. C. P. Michael, M. Borselli, T. J. Johnson, C. Chrystal, and O. Painter, Opt. Express **15**, 4745 (2007).
17. R. S. Daveau, K. C. Balram, T. Pregnolato, J. Liu, E. H. Lee, J. D. Song, V. Verma, R. Mirin, S. W. Nam, L. Midolo, S. Stobbe, K. Srinivasan, and P. Lodahl, Optica **4**, 178 (2017).
18. L. Chang, M. Dijkstra, N. Ismail, M. Pollnau, R. M. de Ridder, K. Wörhoff, V. Subramaniam, and J. S. Kanger, Opt. Express **23**, 22414 (2015).
19. G. Roelkens, D. Van Thourhout, and R. Baets, Opt. Lett. **32**, 1495 (2007).
20. Z. Xiao, T.-Y. Liow, J. Zhang, P. Shum, and F. Luan, Opt. Express **21**, 5688 (2013).
21. W. D. Sacher, Y. Huang, L. Ding, B. J. Taylor, H. Jayatilleka, G. Q. Lo, and J. K. Poon, Opt. Express **22**, 10938 (2014).
22. L. He, Y. Liu, C. Galland, A. E.-J. Lim, G.-Q. Lo, T. Baehr-Jones, and M. Hochberg, IEEE Photonics Technol. Lett. **25**, 1358 (2013).
23. Y. Wang, W. Shi, X. Wang, Z. Lu, M. Caverley, R. Bojko, L. Chrostowski, and A. F. Jaeger, Opt. Lett. **40**, 4647 (2015).
24. D. Benedikovic, C. Alonso-Ramos, P. Cheben, J. H. Schmid, S. Wang, D. X. Xu, J. Lapointe, S. Janz, R. Halir, A. Ortega-Monux, and J. G. Wangüemert-Pérez, Opt. Lett. **40**, 4190 (2015).
25. K. Shastri and F. Monticone, EPJ Appl. Metamat. **9**, 16 (2022).
26. M. Jang, Y. Horie, A. Shibukawa, J. Brake, Y. Liu, S. M. Kamali, A. Arbabi, H. Ruan, A. Faraon, and C. Yang, Nat. Photonics **12**, 84 (2018).
27. A. Yulaev, W. Zhu, C. Zhang, D. A. Westly, H. J. Lezec, A. Agrawal, and V. Aksyuk, ACS Photonics **6**, 2902 (2019).
28. J. Fischer and M. Wegener, Laser Photonics Rev. **7**, 22 (2013).
29. P. Dietrich, M. Blaicher, I. Reuter, M. R. Billah, T. Hoose, A. Hofmann, C. Caer, R. Dangel, B. Offrein, U. Troppenz, M. Moehrle, W. Freude, and C. Koos, Nat. Photonics **12**, 241 (2018).
30. H. Gehring, M. Blaicher, W. Hartmann, P. Varytis, K. Busch, M. Wegener, and W. H. P. Pernice, APL Photonics **4**, 010801 (2019).
31. H. Gehring, A. Eich, C. Schuck, and W. H. Pernice, Opt. Lett. **44**, 5089 (2019).
32. S. Lightman, O. Porat, G. Hurvitz, and R. Gvishi, Opt. Lett. **47**, 5248 (2022).
33. S. Singer, Y. Xu, S. T. Skacel, H. Zwickel, P. Maier, P. I. Dietrich, M. Kaschel, C. Menzel, S. Randel, W, Freude, and C. Koos, Opt. Express **30**, 46564 (2022).
34. L. Wang, Y. Luo, Z. Liu, X. Feng, and B. Lu, Appl. Surf. Sci. **442**, 417 (2018).
35. E. A. Sanchez, M. Waldmann, and C. B. Arnold, Appl. Opt. **50**, 1974 (2011).
36. Z. Wang, T. Li, A. Soman, D. Mao, T. Kananen, and T. Gu, Nat. Commun. **10**, 1 (2019).
37. https://www.nscrypt.com/precision-micro-dispensing/

128.175.82.41 {ts '2023-05-03 15:10:50'}